RESEARCH ARTICLE

WILEY

Image reconstruction for diffuse optical tomography using bi-conjugate gradient and transpose-free quasi minimal residual algorithms and comparison of them

Gençay Sevim[1,2,3] | Yiğit Ali Üncü[3] | Tanju Mercan[3] | Murat Canpolat[3]

[1]Department of Advanced Technology, Graduate School of Science, Eskisehir Technical University, Eskisehir, Turkey

[2]Vocational School of Health Services, Biophysics, Ufuk University, Ankara, Turkey

[3]Biomedical Optics Research Unit, Department of Biophysics, School of Medicine, Akdeniz University, Antalya, Turkey

Correspondence
Gençay Sevim, Department of Advanced Technology Graduate School of Science, Eskisehir Technical University Eskisehir 26555, Turkey.
Email: gencay.sevim@ufuk.edu.tr; gncy.svm@gmail.com

Abstract

Diffuse optical tomography (DOT) is a new emerging modality in the diagnosis of soft tissue abnormalities. DOT image quality substantially depends on the reconstruction stage. In the literature, there are many reconstruction algorithms used in DOT systems. However, some algorithms were improved for solving specific cases but still need to be improved. The bi-conjugate gradient (BiCG) enhanced is one of the conjugate gradient (CG)-based reconstruction techniques for non-Hermitian systems. The BiCG provides a solution to a non-Hermitian system. However, it has erratic convergence in some cases. Therefore, DOT images reconstructed by BiCG can be at the wrong location and is inaccurate in some cases. In this study, we used continuous-wave diffuse optical tomography (CW-DOT) to acquire measurements from breast tissue phantoms with single or double inclusion at different depths and center-to-center separations and we have used the transpose free quasi minimal residual (TFQMR) reconstruction algorithm, improved as an alternative to BiCG for the first time in the CW-DOT system. Moreover, we have experimentally proved that TFQMR is superior to BiCG in some specific cases for the first time in CW-DOT. Therefore, we concluded that TFQMR has the potential to be able to be used in the reconstruction stage in CW-DOT.

KEYWORDS
bi-conjugate gradient, diffuse optical tomography, image reconstruction, reconstruction techniques, transpose free quasi minimal residual

1 | INTRODUCTION

Breast cancer is one of the most common diseases worldwide, and its early diagnosis could increase the effectiveness of treatment and reduce mortality significantly. Currently, the used diagnostic techniques for breast cancer detection are mammography, ultrasonography, and magnetic resonance tomography; however, all these techniques have limitations.[1,2] Therefore, developing a noninvasive breast imaging technique to detect breast cancer is a necessity. One of those techniques is diffuse optical tomography (DOT), used for imaging biological tissues such as the brain and breast.[3-15] Unlike others, DOT is inexpensive and harmless for patients because of using near-infrared light.

The optical properties of biological tissues can be characterized by in terms of absorption (μ_a) coefficient, scattering (μ_s) coefficient, anisotropy, and refractive indexes of tissues.[11] DOT uses the optical properties of blood distribution of tissue to create an image. DOT systems use many reconstruction algorithms to image tissue, and also the reconstructed images are processed to

increase the image quality. Although there are many reconstruction algorithms, the Krylov subspace reconstruction algorithms are proven to be better to solve large systems of equations than other algorithms.[16-18] The Conjugate Gradient (CG) algorithm[19,20] is one of the most preferred Krylov subspace algorithms used to solve non-Hermitian, positive definite matrix systems. However, it fails to satisfy to solve non-Hermitian matrix systems.

The bi-conjugate gradient method (BiCG) is another CG-based algorithm developed[21] to solve non-Hermitian linear systems. The BiCG algorithm may not work for an approximate solution in some cases.[22,23] Two significant properties of CG-based reconstruction methods are required to produce an approximate solution for non-Hermitian systems. The first property is a minimization over Krylov subspace. The second one is that low and constant storage requirements and work per iteration can be enough to solve the system.[22,23] A CG-based reconstruction algorithm should have these two properties to solve non-Hermitian systems. However, the BiCG developed for solving non-Hermitian systems has only the second one because BiCG iterates based on a Galerkin condition,[21] but not a minimization property. Therefore, the BiCG algorithm shows wild oscillations resulting in irregular convergence behavior and numerical instabilities.[22-25]

Freund and Nachtigal proposed quasi minimal residual (QMR) algorithm to overcome the drawback of the BiCG.[23] The QMR algorithm solves the irregular convergence problem; however, like the BiCG, the QMR algorithm needs the matrix-vector multiplications of coefficient matrix (A) and its transpose (A^T) to solve a linear equation.[23] It is a disadvantage. Therefore, the transpose free implementation quasi minimal residual (TFQMR), which does not need any matrix–vector multiplication, was developed by Freund.[22] BiCG and TFQMR reconstruction algorithms have never been used as reconstruction algorithms in continuous-wave diffuse optical tomography (CW-DOT) systems and never compared with each other.

In the study, CW-DOT experiments were performed on the breast tissue phantoms, including inclusions at different depths and center-to-center separations and reconstructed by TFQMR and BiCG algorithms to be compared based on the correctly locating the depths of the inclusion and spatial resolution in case of having double inclusion in the tissue phantoms.

2 | MATERIAL AND METHODS

2.1 | Light transport in tissue and solution of diffusion equation

The distribution of light within a tissue depends on the light wavelength, absorption coefficient, scattering coefficient, scattering anisotropy, and refractive indexes and is expressed mathematically and physically by the Radiative transfer equation (RTE) (Equation (1))[11].

$$\frac{\partial L(\vec{r},\hat{s},t)}{c\,\partial t} = -\hat{s}.\nabla L(\vec{r},\hat{s},t) - \mu_t L(\vec{r},\hat{s},t) + \mu_s \int_{4\pi} L(\vec{r},\hat{s},t) P(\hat{s}'.\hat{s}) d\Omega' + S(\vec{r},\hat{s},t) \quad (1)$$

where, c is the speed of light, μ_t is the attenuation coefficient, $P(\hat{s}',\hat{s})$ is the scattering probability density function from $\hat{s}'$ to $\hat{s}$, $S(\vec{r},\hat{s},t)$ is a light source, and $L(\vec{r},\hat{s},t)$ refers to radiance. Since there is no analytical solution of the RTE, it is approximated diffusion equation (DE) (Equation (2)).[11,26,27] DOT systems have three approaches: time-domain, frequency-domain, and continuous-wave.[28] Since our system has been designed as CW-DOT,[29] the DE can be expressed as Equation (2).

$$D\nabla^2\Phi(r) - c\mu_a(r)\Phi(r) = -cS(r) \quad (2)$$

$\Phi(r)$ (W/m^2) is the light flux at the r point. In a DOT system, the DE must be a resolvable form to create a tomographic image. The Born and Rytov approaches, the most basic approaches used in the solution of the DE, should be used to do this.[4,8,30] The Rytov approximation assumes that the light flux is written exponentially as Equation (3).[31,32]

$$\Phi(r) = \Phi_0(r)\exp(\Phi_{scat}(r)), \ \Phi_0(r) \gg \Phi_{scat}(r) \quad (3)$$

$$\mu_a(r) = \mu_{a,0}(r) + \mu_{a,1}(r) \ \mu_{a,0}(r) \gg \mu_{a,1}(r) \quad (4)$$

Φ_0 refers to the measurement obtained from a homogeneous medium. Φ_{scat} refers to the change in the light flux. $\mu_{a,0}$ is the absorption coefficient of the homogeneous medium, and $\mu_{a,1}$ is the difference in the absorption coefficient between the inclusion and the homogeneous medium. Then, Equation (5) is obtained by arranging Equation (3).

$$\Phi_{scat} = \ln\left(\frac{\Phi}{\Phi_0}\right) \quad (5)$$

The DE with Rytov approximation can be again expressed as Equation (6).[32]

$$\Phi_{scat}(r_d, r_s) = -\frac{1}{\Phi_0(r_d, r_s)} \int \frac{G(r-r_d)}{D} c\Delta\mu_a(r)\Phi_0(r, r_s)d^3r \quad (6)$$

$G(r-r_d)$ refers to the Green function of the detector and the voxel, $\Phi_0(r_d, r_s)$ refers to the light flux from the source

to the detector, and $\Phi_0(r,r_s)$ refers to the light flux between the source and the voxel. r_s indicates the position of the source and r_d indicates the position of the detector. Equation (6) can be expressed in a discrete form as Equation (7) to create images based on the attenuation over voxels.

$$-\ln\left(\frac{\Phi}{\Phi_0}\right) = \frac{cV_v}{D}\sum_{j\in\text{voxel}}\Phi_0(r_s,r_j)\Phi_0(r_j,r_d)\Delta\mu_a(r_j) \quad (7)$$

V_v indicates the volume of the voxel and r_j indicates the position of the voxels. $\Phi_0(r_s,r_j)$ refers to the light flux from a source to a jth voxel, and $\Phi_0(r_j,r_d)$ refers to the light flux from jth voxel to a detector. Then, $\Phi_0(r_s,r_j)$ and $\Phi_0(r_j,r_d)$ are arranged as the following:

$$A_{i,j} = \Phi_{\text{source}}(r_{s_i},r_j)\Phi_{\text{dedector}}(r_j,r_{d_i}). \quad (8)$$

$A_{i,j}$ defines the weight function between ith source and jth detector over all the voxels. r_{s_i} is ith source position, r_{d_i} is ith detector position and r_j is jth voxel position. Combining Equation (8) and Equation (7) provides Equation (9).

$$\begin{bmatrix} y_1 \\ \vdots \\ y_M \end{bmatrix} = -\frac{cV_v}{D}\begin{bmatrix} A_{1,1} & \cdots & A_{1,N} \\ \vdots & \ddots & \vdots \\ A_{M,1} & \cdots & A_{M,N} \end{bmatrix}\begin{bmatrix} \Delta\mu_a(r_1) \\ \vdots \\ \Delta\mu_a(r_N) \end{bmatrix} \quad (9)$$

$y_1, y_2,..., y_M$ is perturbation data $(\ln\left(\frac{\Phi}{\Phi_0}\right))$ obtained from the homogenous and non-homogeneous medium. $[\Delta\mu_a(r_1), \Delta\mu_a(r_2), ..., \Delta\mu_a(r_n)]$ refers to a change in the absorption coefficients from the background for each voxel. M is the measurement number, N is the total number of voxels. Since c, D, and V_v are not variables, this part is defined as below.

$$A \equiv -\frac{cV_v}{D}\begin{bmatrix} A_{1,1} & \cdots & A_{1,N} \\ \vdots & \ddots & \vdots \\ A_{M,1} & \cdots & A_{M,N} \end{bmatrix} \quad (10)$$

Then, Equation (9) can be expressed as a linear equation (Equation (11)) using Equation (10).[8,30] The equation is defined mathematically as a forward problem.

$$y = Ax \quad (11)$$

It is necessary to solve the inverse problem (Equation (12)) to reconstruct an image in our DOT.

$$x = A^{-1}y \quad (12)$$

y is a measurement data called perturbation data, A is a coefficients matrix obtained using Monte Carlo simulations,[29] and x is a matrix of unknowns representing a distribution of the absorption coefficients in Equation (12).

2.2 | Reconstruction algorithms

In obtaining tomographic images in the CW-DOT systems, many reconstruction algorithms solve the inverse problem. However, Krylov subspace reconstruction algorithms provide a better solution to large, sparse scale systems of equations.[16-18] We have used two subspace algorithms to solve the inverse problem with non-Hermitian data in the study. One of them is BiCG, developed for solving non-hermitian systems. Another one is TFQMR, an improved version of QMR.

2.2.1 | Bi-conjugate gradient

The CG algorithm[19,20] provides a smooth convergence for large, sparse, and non-Hermitian matrix systems. It produces residual (r) (Equations (14) and (16)), search (p) (Equations (13) and (15)), and unknowns (x) vectors per each iteration to solve the system. It uses search vectors (p) obtained by using residuals (r) (Equation (16)), namely that the working principle of the CG is to use the subspace (Equations (13) and (14)) to reach the solution. For the CG algorithm, see the Ref. 19.

$$P_i = \text{span}(p_0, Ap_0, A^2p_0,...,A^{i-1}p_0) \quad (13)$$

$$= \text{span}(r_0, Ar_0, A^2r_0,...,A^{i-1}r_0) \quad (14)$$

$$p_{i+1} := r_{i+1} + \beta_{i+1}p_i \quad (15)$$

$$r_{i+1} := r_i - \alpha_i Ap_i \quad (16)$$

α is a constant of orthogonality relation, and β is Gram-Schmidt constant. Although the CG provides the solution for such a system, it is not satisfied with the non-Hermitian system because A must be symmetric and positive-definite. Therefore, the BiCG was improved to solve the non-Hermitian system.[33] The BiCG uses the same subspaces with CG but another subspace defined in Equation (17), which is orthogonal to the P_i subspace.

$$L_i = \text{span}\left(w_0, A^T w_0, (A^T)^2 w_0, ..., (A^T)^{i-1} w_0\right) \quad (17)$$

Therefore, the BiCG does not need a symmetric coefficient matrix while solving a system. The BiCG uses additional two vectors (Equations (18) and (19)) being intrinsic to L_i subspace, in addition to others in CG (Equations (15) and (16)).

$$r_i^* = r_{i-1}^* - \alpha_i A^T p_i^* \quad (18)$$

$$p_i^* = r_{i-1}^* - \beta_i p_{i-1}^* \quad (19)$$

In reaching the solution, the BiCG continues iteration until it finds a suitable vector fulfilling the following conditions;

$$(r_i^*, r_j) = 0, i \neq j \quad (20)$$

$$(p_i^*, A p_j) = 0, i \neq j \quad (21)$$

Although the BiCG algorithm was created for non-Hermitian systems, it is numerically unstable due to wild oscillation results in irregular convergence behavior.[22,23] For the detailed BiCG algorithm, see the Ref. 21,34 or Supporting Information.

2.2.2 | Transpose free quasi minimal residual

Freund and Nachtigal have proposed the QMR[23-25] for solving the irregular convergence behavior problem systems of linear equations. The QMR method based on the non-symmetric Lanczos process requires matrix–vector multiplications with the A and A^T to obtain a solution.[22-25]

$$v_1, w_1 \in \mathbb{C}^N, \text{with } \|v1\| = \|w1\| = 1 \quad (22)$$

$$\text{span}\{v_1, v_2, ..., v_n\} = K_n(v_1, A) \quad n = 1, 2, ... \quad (23)$$

$$\text{span}\{w_1, w_2, ..., w_n\} = K_n(w_1, A^T) \quad n = 1, 2, ... \quad (24)$$

The non-symmetric Lanczos algorithm generates two sequences of vectors $v_1, v_2, ...$ (Equation (23)) and $w_1, w_2, ...$ (Equation (24)) by starting with initial vectors (Equation (22)) for $n = 1, 2, ...$; hence, it requires transpose of the coefficient matrix. Thus, Freund proposed the TFQMR method to overcome the problem by modifying

the QMR algorithm.[22] A non-singular matrix satisfying the following condition (Equation (25)) is used to choose the second initial vector arbitrarily w_1 (Equation (26)). Also, the non-singular matrix is used for computing the sequence of vectors w_1, w_2, ... (Equation (27)); hence, A^T can be omitted. For the detailed TFQMR algorithm, see the Ref. 22 or Supporting Information.

$$A^T S = S A, \ S \in \mathbb{C}^{NxN} \quad (25)$$

$$w_1 := \frac{1}{\|Sv_1\|} S v_1 \quad (26)$$

$$w_n = \frac{\gamma_n}{\|Sv_1\|} S v_n = \frac{1}{\|Sv_n\|} S v_n \quad (27)$$

2.3 | CW-DOT system

In the CW-DOT system, a diode laser with a wavelength of 808 nm was used. The CW-DOT system consists of 49 detectors and 49 source fibers embedded in the matrix of 10×10. The light is delivered to the tissue phantom with the source fibers sequentially, and back-reflected light is detected at the same time by all detector fibers.[5] In Figure 1, the system is shown schematically.

2.4 | In-vitro experiments

In-vitro measurements acquired from a tissue phantom consists of a mixture of pure water, Intralipid, and Indocyanine Green (ICG). For the tissue phantom, a $30 \times 15 \times 20$ cm intralipid-water tank was designed using black Delrin to avoid reflection light from the surfaces (Figure 2).

Scattering and absorption coefficients of the tissue phantom were 10 cm^{-1} and 0.004 cm^{-1} at 808 nm. In the literature, the absorption coefficient of the breast tissue at 635 nm is smaller than 0.2 cm^{-1}[35]; however, we determined 0.004 cm^{-1} at 808 nm to model breast tissue because a breast generally consists of fat tissues and the absorption coefficient of fat tissue at approximately 800 nm is 0.004 cm^{-1}. We utilized from Oregon Medical Laser Center (OMLC) for this (https://omlc.org/spectra/fat/, Date Accessed: January 20, 2021).

ICG was used to enable the phantom and inclusions to show the optical properties of the breast tissue and tumors, respectively. First, a mixture of ICG and pure water was prepared using the following calculations (Equations (28)–(30)). It is known that the absorption
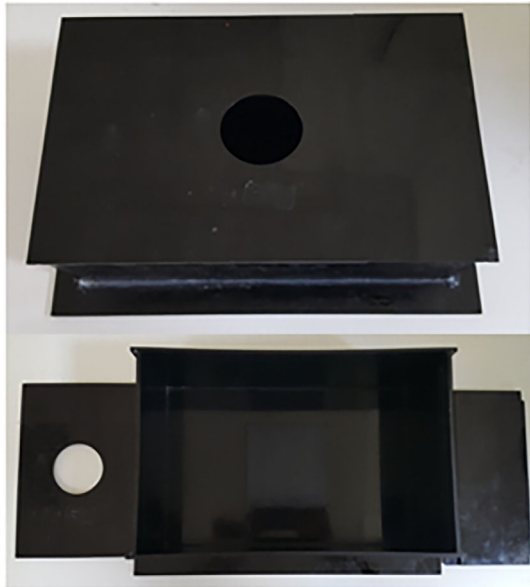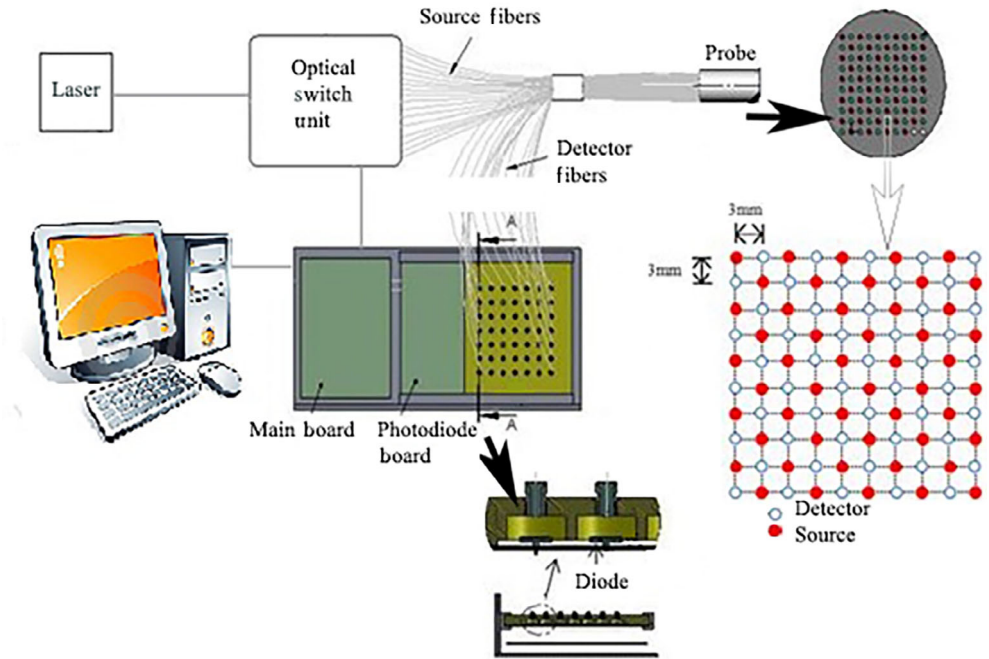
FIGURE 2   Water–intralipid tank [Color figure can be viewed at wileyonlinelibrary.com]

coefficient of a 10 μM ICG solution for a light at 808 nm wavelength is 3.419 cm^{-1} and its molecular weight is 775 g. With this information, the molarity formula was utilized to calculate the ICG mass used for preparing the phantom and inclusions model of tumors.

$$M = \frac{n}{V} \tag{28}$$

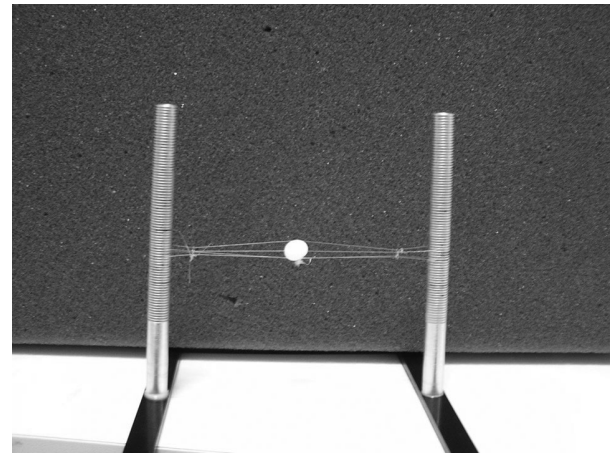M is molarity, n is moles, and V is volume.

FIGURE 3   Inclusion made by a mixture of 1% Intralipid, pure water, and ICG

$$n = \frac{m}{M_a} \tag{29}$$

m is mass, M_a is molecular weight.

Equation (30) is obtained using Equations (28) and (29).

$$m = MVM_a \tag{30}$$

The amount of pure water required to be added per 1 mg of ICG to form the ICG–water solution was determined using Equation (30). In this way, 10 μM solution was prepared with 1 mg ICG and 129 mL pure water. Then, 5000 mL of intralipid and ICG–water mixture was

prepared within the intralipid tank. The required molarity was calculated firstly for the absorption coefficient of this mixture to be 0.004 cm^{-1}. Then, it was decided at what ratio the ICG–water mixture to be added according to this molarity.

After preparing the breast phantom similar to breast tissue, inclusions were created. That the angiogenesis around the tumorous structures is more intense than the normal tissue causes the absorption coefficient of tumors to be higher than the normal breast tissue. Based on this, we utilized hemoglobin data of OMLC (https://omlc.org/spectra/, Date Accessed: January 20, 2021). Thus, we determined the absorption coefficient of inclusions to be 0.016 cm^{-1}. The same procedures applied when creating the phantom were also followed to create inclusions.

The absorption coefficient of the phantom and inclusions were measured using a UV–VIS spectrometer. The average absorption coefficients of the phantom and inclusions were approximately 0.004 and 0.016 cm^{-1}, respectively. The inclusions were prepared by filling a transparent balloon with the intralipid–ICG–water mixture (Figure 3).

The inclusion was placed at a depth of 0.7 cm and then 1.5 cm in the breast phantom. Then, the data was obtained using the DOT system, and it was used in the reconstruction stage to compare the depth-dependent resolutions of both algorithms. In both depths, the inclusion was at the center of the x–y plane of the optical fiber probe. Then, two inclusions with center-to-center distances of 2 cm were placed at a depth of 0.9 cm to investigate the algorithms' ability in imaging the two inclusions.
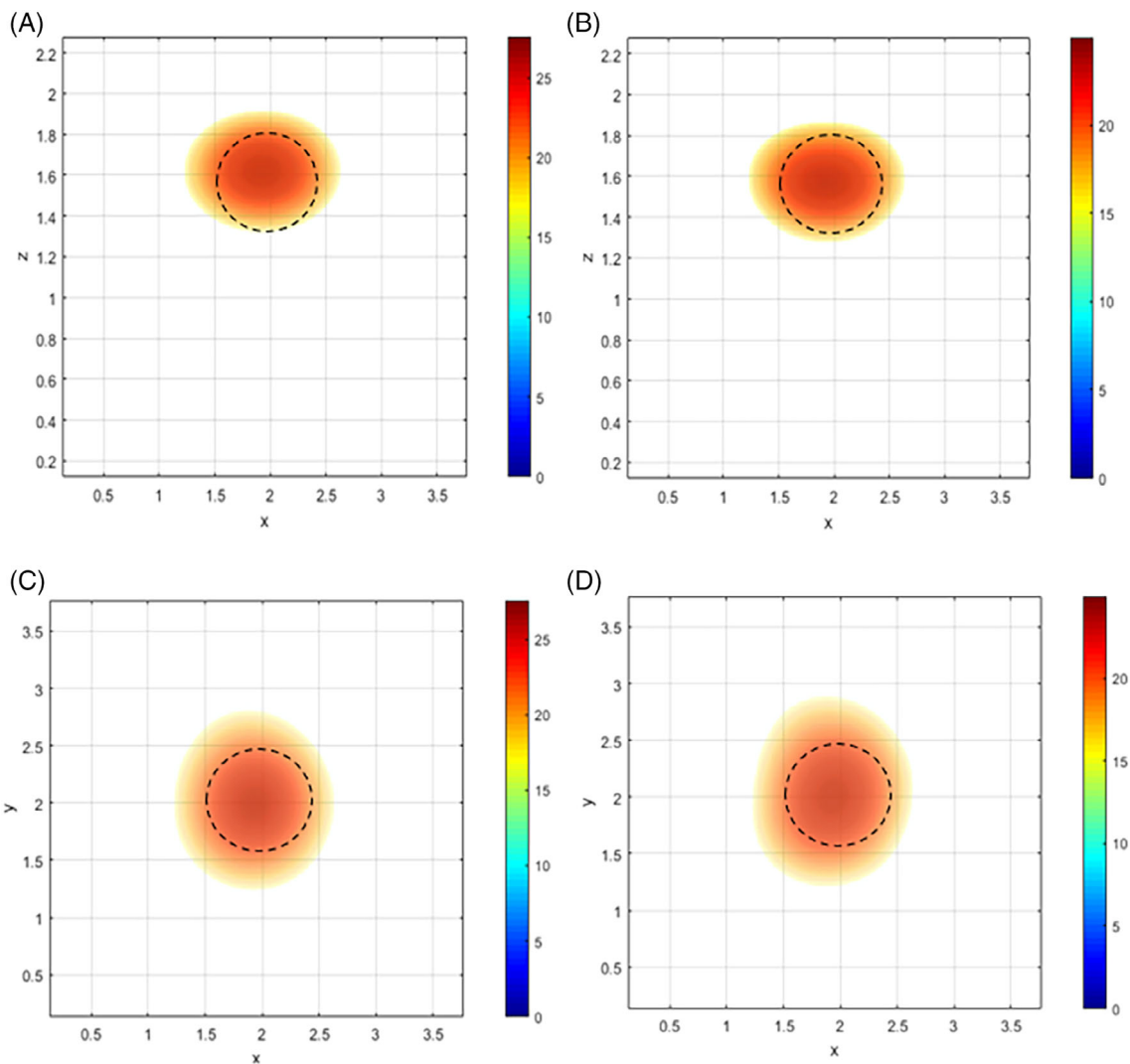

FIGURE 4 Reconstructed images of the tissue phantom with the inclusion at a depth of approximately 0.7 cm. (A) and (C) are the presentation of the inclusion in the X–Z plane and the X–Y plane reconstructed by BiCG. (B) and (D) are the presentation of the inclusion in the X–Z plane and X–Y plane reconstructed by TFQMR. The dashed line circles indicate the actual size and location of the inclusion. Color bars represent the change of absorption coefficient [Color figure can be viewed at wileyonlinelibrary.com]

3 | RESULTS

The source and detector fibers cannot transmit light at the same level intensity. Namely, the distance between the different source-detector pairs with the same neighborhood is different from each other even if it is tiny; thus, all source and detector fibers cannot carry the light with the same intensity. Therefore, calibration measurements were taken on the phantom without any inclusion at first. After taking these measurements, inclusions were placed carefully into this at the desired locations in the phantom. After taking the measurements, the system was calibrated. At this stage, before being entered into any reconstruction process, the measurements taken with the DOT system were divided into the calibration data taken without inclusion in the intralipid (Equation (31)).

$$R = \frac{M_{\text{measurement}}}{M_{\text{calibration}}} \tag{31}$$

$M_{\text{measurement}}$ is the measurement with inclusion, and $M_{\text{calibration}}$ is the data taken on a homogeneous mixture without inclusion. In this way, the calibrated data (R) is made independent of the light-emitting and light-collecting efficiency of the fibers.

The inclusions were placed at different depths and locations within the phantom after the calibration measurements were performed. Then, data acquired from the
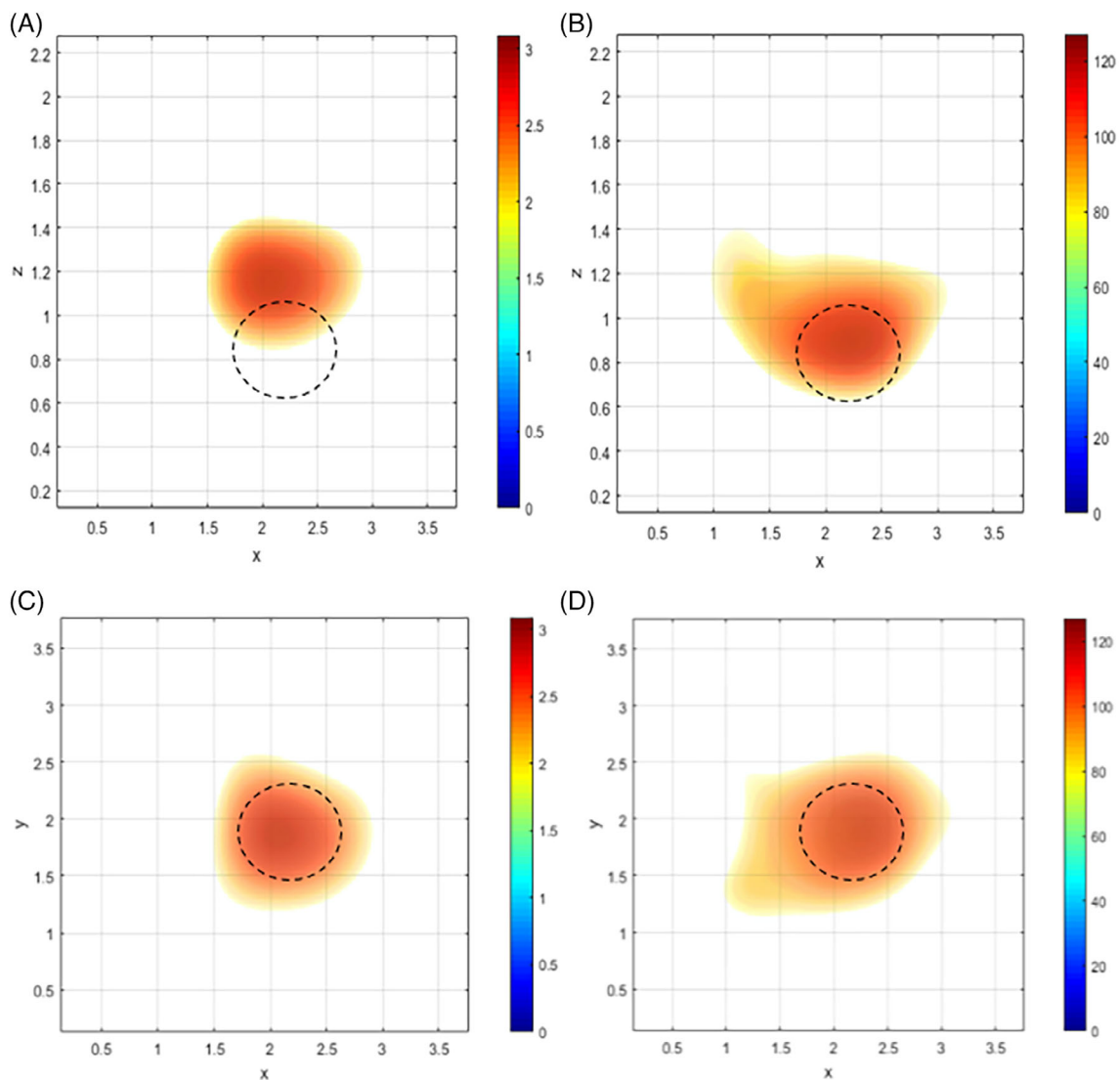

FIGURE 5 Reconstructed images of the tissue phantom with the inclusion at a depth of approximately 1.5 cm. (A) and (C) are of presentation of the inclusion in the X–Z plane and X–Y plane reconstructed by BiCG. (B) and (D) are the presentation of the inclusion in the X–Z plane and X–Y plane reconstructed by TFQMR. The dashed line circles indicate the actual size and location of inclusion. Color bars represent the change of absorption coefficient [Color figure can be viewed at wileyonlinelibrary.com]

phantom by CW-DOT. Data acquired from the tissue phantoms, including one or two inclusions, were used in the reconstruction process by TFQMR and BiCG.

In the first experiment, the inclusion was placed at a depth of approximately 0.7 cm. Then, the tissue phantom was reconstructed by both algorithms. As seen in Figure 4, the depth of the inclusion is 0.68 and 0.70 cm at the images reconstructed by BiCG and TFQMR, respectively. The difference between the depth of the images is 0.02 cm and negligible.

In the second experiment, the inclusion was placed at a depth of approximately 1.5 cm. As seen in Figure 5(A), the inclusion is not at its actual depth, nearly 4 mm above its actual location in the image reconstructed by BiCG. However, the image produced by BiCG is the more

similar shape of the inclusion. Even though the TFQMR algorithm reconstructs a dispersed image (Figure 5(B,D)), the inclusion is at its actual depth.

In the third experiment, two inclusions were placed at a depth of approximately 0.9 cm with a center-to-center separation of approximately 2 cm to test the accuracy of both reconstruction algorithms. The TFQMR was observed to reconstruct a more accurate image than BiCG. In the TFQMR-reconstructed image, the two inclusions are at correct locations, and they seem to separate from each other (Figure 6(B,D)). In the BiCG-reconstructed images, one of the inclusions is unclear, although one is accurately seen (Figure 6(A,C)).

In the fourth experiment, two inclusions were placed at a depth of approximately 0.7 cm with center-to-center
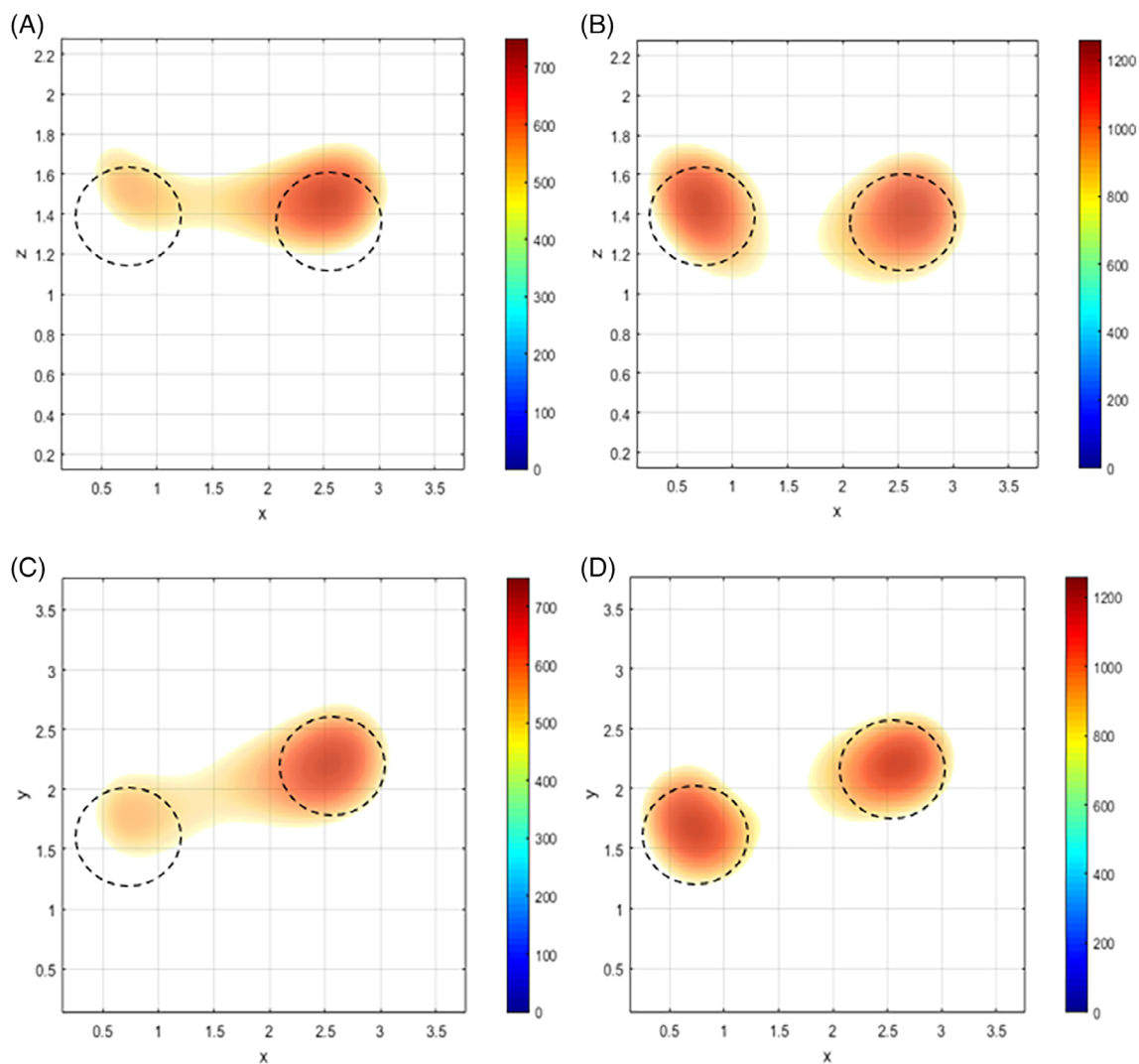

FIGURE 6 Reconstructed images of the tissue phantom with two inclusion inclusions at a depth of approximately 0.9 cm and center-to-center distance of approximately 2 cm. (A) and (C) are of presentation of the inclusions in the X–Z plane and X–Y plane reconstructed by BiCG. (B) and (D) are the presentation of the inclusions in the X–Z plane and X–Y plane reconstructed by TFQMR. The dashed line circles indicate the actual size and location of inclusion. Color bars represent the change of absorption coefficient [Color figure can be viewed at wileyonlinelibrary.com]

separation of approximately 1.4 cm which is 0.6 cm smaller than the separation of the third experiment. As seen in Figure 7, TFQMR created a more accurate image again than BiCG. BiCG created an unclear image (Figure 7 (A,C)).

In the fifth experiments, the inclusion was placed at a depth of approximately 0.9 cm. As seen in Figures 4, 5, and 8, depth is a significant parameter affecting to be reconstructed an image correctly. Like the second experiment, TFQMR created an image with the correct location again (Figure 8), although it is a dispersed image.

In all the experiments, the single inclusion was placed to three different depths, and double inclusions were placed to two different depths with two different center-to-center separations. Then, CW-DOT data, acquired from the tissue phantoms, were reconstructed by TFQMR and BiCG. These experiments confirm the superiority of the TFQMR algorithm over BiCG in determining the actual depth of inclusion. Although the TFQMR requires a higher number of iterations than the BiCG, it has provided better solutions in cases where the matrix structure is inconvenient to solve.

4 | DISCUSSION

There are three approaches for accomplishing DOT; time-domain, frequency-domain, and continuous-wave. Each approach has disadvantages and advantages. CW-DOT systems are less expensive, but their image quality is lower than the others. It is the most significant disadvantage of it and needed to be solved. Therefore, we focused on reconstruction, one of the most critical processes affecting image quality.
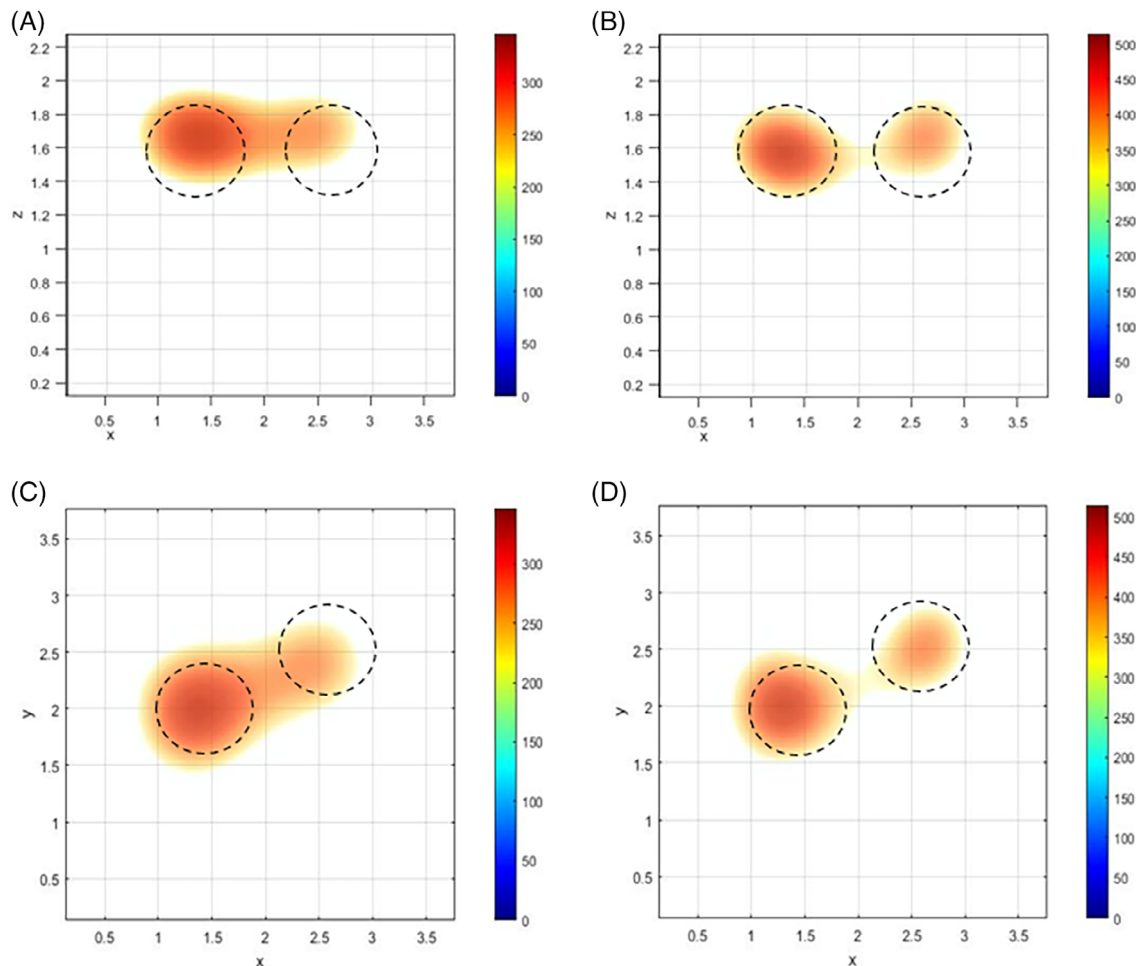

FIGURE 7 Reconstructed images of the tissue phantom with two inclusion inclusions at a depth of approximately 0.7 cm and center-to-center distance of approximately 1.4 cm. (A) and (C) are of presentation of the inclusions in the X–Z plane and X–Y plane reconstructed by BiCG. (B) and (D) are the presentation of the inclusions in the X–Z plane and X–Y plane reconstructed by TFQMR. The dashed line circles indicate the actual size and location of inclusion. Color bars represent the change of absorption coefficient [Color figure can be viewed at wileyonlinelibrary.com]

FIGURE 8 Reconstructed images of the tissue phantom with the inclusion at a depth of approximately 0.9 cm. (A) and (C) are the presentations of the inclusion in the X–Z plane and X–Y plane reconstructed by BiCG. (B) and (D) are the presentations of the inclusion in the X–Z plane and X–Y plane reconstructed by TFQMR. The dashed line circles indicate the actual size and location of inclusion. Color bars represent the change of absorption coefficient [Color figure can be viewed at wileyonlinelibrary.com]
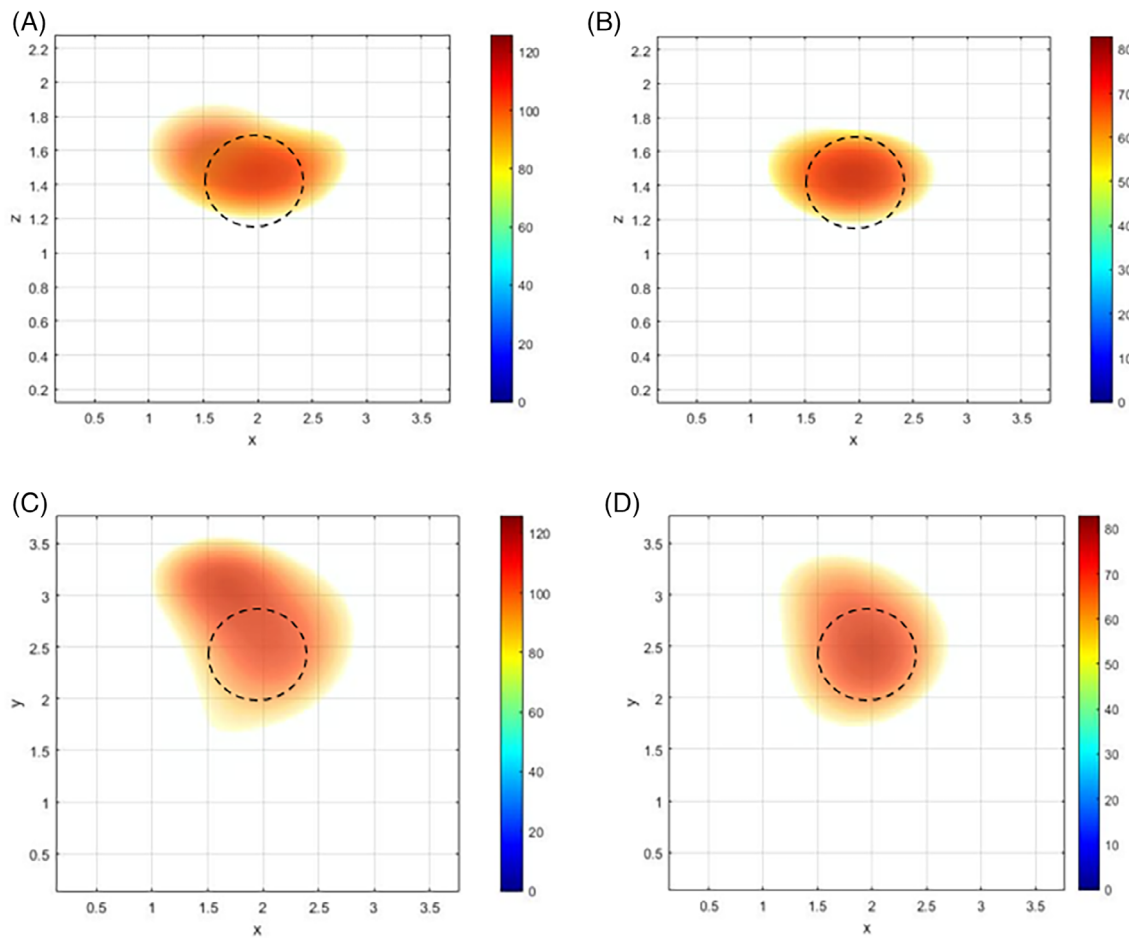
CW-DOT systems use many reconstruction methods to solve large systems. However, CG-typed reconstruction methods are proven to be the most effective iterative method to find a solution of large, sparse, non-Hermitian, positive definite linear systems in CW-DOT systems.[16-19,36] In our previous study, we used Algebraic Reconstruction (ART), Simultaneous Iterative Reconstruction (SIRT), Truncated Singular Value Decomposition (TSVD), and Truncated Conjugate Gradient (TCG) techniques and compared them with each other.[17,18] In the study, we inferred that the TCG technique provides better images for our CW-DOT systems in line with the literature. However, obtaining the correct depth of the inclusions and low spatial resolution were still needed to be improved.

Although the CG technique is one the most powerful technique to solve large sparse linear systems with Hermitian positive definite coefficient matrices, it does not provide a better solution to systems with non-Hermitian,

non-singular matrices.[22-25] The BiCG technique was improved to solve systems with non-Hermitian, non-singular matrices. However, it was proved mathematically to have irregular convergence behavior and may result in breakdowns. In solving non-Hermitian systems, a CG-based reconstruction algorithm must possess two significant properties. These properties are the generating iterations defined by minimization over Krylov-subspace, and the computing with low and constant storage requirements and less work per iteration.[23-25] However, the BiCG algorithm provides only the second one because the iteration step of the BiCG is defined as a Galerkin condition but not minimization.[21,23,34] Therefore, the BiCG can exhibit wild oscillatory residual behavior being irregular converged. Freund and Nachtigal put forward the QMR technique providing smooth convergence behavior to overcome the problem.[23] Unlike the BiCG, the iteration of the QMR is defined as a minimization property, called a quasi-minimal residual property.

Therefore, the QMR converges smoother than the BiCG. However, like the BiCG, the QMR needs multiplications of the coefficient matrix and its transpose to generate a solution.[22,23] Although the QMR exhibits smooth convergence, the multiplications put it at a disadvantage in some cases. For this disadvantage, the Conjugate Gradient Squared (CGS) technique was proposed by Sonneveld.[37] The CGS does not need a matrix–vector multiplication of a coefficient matrix with its transpose. However, like the BiCG, the CGS iterates are also characterized by a Galerkin condition; thus, it exhibits irregular convergence behavior. Freund proposed the TFQMR technique for solving these problems and disadvantages.[22] The TFQMR is different from the QMR technique mathematically. The TFQMR was derived by changing two vector sequences used in the CGS. Although TFQMR needs more iterates than BiCG, it provides smooth convergence. Therefore, we integrated it into our CW-DOT system and tested it.

BiCG and TFQMR have been used in the CW-DOT system for the first time, and it has been first time experimentally proved that the TFQMR algorithm is better than BiCG for difficult situations in this study. For the test, we performed some experiments in which the CG-based algorithm is insufficient to reconstruct. Although TFQMR provides images with similar quality in some cases, it offers images with better quality in difficult conditions. Because the breast has more complex and heterogeneous than one modeling breast tissue in the intralipid experiments, it has shown which is more convenient to be used as the reconstruction algorithm of clinical CW-DOT systems.

5 | CONCLUSION

We have compared TFQMR and BiCG reconstruction algorithms with each other in a CW-DOT system. Both algorithms have been used to reconstruct CW-DOT data acquired from the tissue phantoms at different depths and with multiple inclusions (Figures 4–8). It has been shown that TFQMR provides images in the correct location, but BiCG not. We have also observed that TFQMR can create more accurate images of multiple inclusions with a better spatial resolution than BiCG. We have experimentally shown at the first time that TFQMR has the potential to be used in CW-DOT systems.

6 | FUTURE WORK

In this article, the TFQMR algorithm has been shown to provide a better solution to low accuracy problems in DOTs images. However, data were obtained from a breast phantom with inclusions modeling tumor. We are planning to reconstruct ex-vivo breast phantom imaging and clinical breast imaging using the TFQMR algorithm.

CONFLICT OF INTEREST
The authors declare no conflicts of interest.

AUTHOR CONTRIBUTION
Gençay Sevim: Part of this study is his thesis. Processed the raw image data and developed the reconstruction algorithms for the DOT system. **Yiğit Ali Üncü:** Processed the images and took the raw image data. **Tanju Mercan:** Worked on the calibration of the system and took the raw image data. **Murat Canpolat:** Designed and developed the DOT system.

DATA AVAILABILITY STATEMENT
Data available on request from the authors.

ORCID
Gençay Sevim https://orcid.org/0000-0002-2157-3209
Yiğit Ali Üncü https://orcid.org/0000-0001-7398-9540
Tanju Mercan https://orcid.org/0000-0002-6711-6003
Murat Canpolat https://orcid.org/0000-0003-3298-9725

REFERENCES
1. Heywang-Köbrunner SH, Hacker A, Sedlacek S. Advantages and disadvantages of mammography screening. *Breast Care*. 2011;6(3):2. https://doi.org/10.1159/000329005.
2. Wang L. Early diagnosis of breast cancer. *Sensor*. 2017;17(7): 157. https://doi.org/10.3390/s17071572.
3. Aminoto T, Priambodo PS, Sudibyo H. (2019) Optical imaging for human body medical analysis using polychromatic infrared LED 700-1100nm. In: AIP Conference Proceedings. https://doi.org/10.1063/1.5139377.
4. Boas DA, Brooks DH, Miller EL, et al. Imaging the body with diffuse optical tomography. *IEEE Signal Process Mag*. 2001;18 (6):57-75. https://doi.org/10.1109/79.962278.
5. Canpolat M, Kazanci HÖ, Mercan T, Alimoğlu E. Design of breast laser tomography system and pilot clinical results. *Akdeniz Med J*. 2015;1(1):58-63. https://doi.org/10.17954/amj.2015.07.
6. Carbone NA, Baez GR, García HA, et al. Diffuse reflectance optical topography: location of inclusions in 3D and detectability limits. *Biomed Opt Express*. 2014;5(5):1336. https://doi.org/10.1364/boe.5.001336.
7. Chae EY, Kim HH, Sabir S, et al. Development of digital breast tomosynthesis and diffuse optical tomography fusion imaging for breast cancer detection. *Sci Rep*. 2020;10(1):13127. https://doi.org/10.1038/s41598-020-70103-0.
8. Durduran T, Choe R, Baker WB, Yodh AG. Diffuse optics for tissue monitoring and tomography. *Rep Prog Phys*. 2010;73(7): 076701. https://doi.org/10.1088/0034-4885/73/7/076701.
9. Eggebrecht AT, Ferradal SL, Robichaux-Viehoever A, et al. Mapping distributed brain function and networks with diffuse optical tomography. *Nat Photon*. 2014;8(6):448-454. https://doi.org/10.1038/nphoton.2014.107.

10. Grosenick D, Rinneberg H, Cubeddu R, Taroni P. Review of optical breast imaging and spectroscopy. *J Biomed Opt*. 2016;21 (9):091311. https://doi.org/10.1117/1.jbo.21.9.091311.

11. Hoshi Y, Yamada Y. Overview of diffuse optical tomography and its clinical applications. *J Biomed Opt*. 2016;21(9):091312. https://doi.org/10.1117/1.jbo.21.9.091312.

12. Liu C, Maity AK, Dubrawski AW, Sabharwal A, Narasimhan SG. (2020) High resolution diffuse optical tomography using short range indirect subsurface imaging. In: IEEE International Conference on Computational Photography, ICCP 2020. https://doi.org/10.1109/ICCP48838.2020.9105173.

13. Prakash J, Shaw CB, Manjappa R, Kanhirodan R, Yalavarthy PK. Sparse recovery methods hold promise for diffuse optical tomographic image reconstruction. *IEEE J Sel Top Quantum Electron*. 2014;20(2):74-82. https://doi.org/10.1109/JSTQE.2013.2278218.

14. Sabir S, Cho S, Heo D, Hyun Kim K, Cho S, Pua R. Data-specific mask-guided image reconstruction for diffuse optical tomography. *Appl Optics*. 2020;59(30):9328. https://doi.org/10.1364/ao.401132.

15. Yoo J, Sabir S, Heo D, et al. Deep learning diffuse optical tomography. *IEEE Trans Med Imaging*. 2020;39(4):877-887. https://doi.org/10.1109/TMI.2019.2936522.

16. Gaudette RJ, Brooks DH, CA DM, et al. A comparison study of linear reconstruction techniques for diffuse optical tomographic imaging of absorption coefficient. *Phys Med Biol*. 2000; 45(4):1051-1070. https://doi.org/10.1088/0031-9155/45/4/318.

17. Mercan, T., Sevim, G., Kazancı, H. Ö., Üncü, Y. A., & Canpolat, M (2018) Comparison of images produced by diffuse optical tomography with two different backscatter techniques. In: 2017 21st National Biomedical Engineering Meeting, BIYOMUT 2017. https://doi.org/10.1109/BIYOMUT.2017.8479038.

18. Mercan T, Sevim G, Üncü YA, Uslu S, Kazanci HÖ, Canpolat M. The comparison of reconstruction algorithms for diffuse optical tomography. *Süleyman Demirel Üniv Fen Edebiyat Fakült Fen Derg*. 2019;14(2):285-295.

19. Gutknecht MH. A brief Introduction to Krylov space methods for solving linear systems. *Front Comput Sci*. 2007;53-62. https://doi.org/10.1007/978-3-540-46375-7_5.

20. Hestenes MR, Stiefel E. Methods of conjugate gradients for solving linear systems. *J Res Natl Bur Stand*. 1952;49(6):409. https://doi.org/10.6028/jres.049.044.

21. Bank RE, Chan TF. A composite step bi-conjugate gradient algorithm for nonsymmetric linear systems. *Numer Algorithms*. 1994;7(1):1-16. https://doi.org/10.1007/BF02141258.

22. Freund RW. A transpose-free quasi-minimal residual algorithm for non-Hermitian linear systems. *SIAM J Sci Comput*. 1993;14 (2):470-482. https://doi.org/10.1137/0914029.

23. Freund RW, Nachtigal NM. QMR: a quasi-minimal residual method for non-Hermitian linear systems. *Numer Math*. 1991; 60(1):315-339. https://doi.org/10.1007/BF01385726.

24. Freund RW, Nachtigal NM. (1994a) A new Krylov-subspace method for symmetric indefinite linear systems. In: Proceedings of the 14th IMACS World Congress on Computational and Applied Mathematics. https://doi.org/10.2172/10190810.

25. Freund RW, Nachtigal NM. An implementation of the QMR method based on coupled two-term recurrences. *SIAM J Sci Comput*. 1994;15(2):313-337. https://doi.org/10.1137/0915022.

26. Farrell TJ, Patterson MS, Wilson B. A diffusion theory model of spatially resolved, steady-state diffuse reflectance for the noninvasive determination of tissue optical properties in vivo. *Med Phys*. 1992;19(4):879-888. https://doi.org/10.1118/1.596777.

27. Haskell RC, Svaasand LO, Tsay TT, Feng TC, McAdams MS, Tromberg BJ. Boundary conditions for the diffusion equation in radiative transfer. *J Opt Soc Am A*. 1994;11(10):2727. https://doi.org/10.1364/josaa.11.002727.

28. Gibson AP, Hebden JC, Arridge SR. Recent advances in diffuse optical imaging. *Phys Med Biol*. 2005;50(4):R1-R43. https://doi.org/10.1088/0031-9155/50/4/R01.

29. Kazanci HÖ, Mercan T, Canpolat M. Design and evaluation of a reflectance diffuse optical tomography system. *Opt Quantum Electron*. 2015;47(2):257-265. https://doi.org/10.1007/s11082-014-9910-6.

30. Choe R, Durduran T. Diffuse optical monitoring of the neo-adjuvant breast cancer therapy. *IEEE J Sel Top Quantum Electron*. 2012;18(4):1367-1386. https://doi.org/10.1109/JSTQE.2011.2177963.

31. Arridge SR. Optical tomography in medical imaging. *Inverse Problems*. 1999;15(2):R41-R93. http://doi.org/10.1088/0266-5611/15/2/022.

32. White, B. (2012) Developing high-density diffuse optical tomography for neuroimaging [dissertation]. St. Louis: Washington University.

33. Fletcher R. Conjugate gradient methods for indefinite systems. In: Watson G, ed. *Numerical analysis*. Berlin, Heidelberg: Springer; 1976;506:73-89.

34. Ortega G, Vázquez F, Garzon EM, García Fernandez I. The BiConjugate gradient method on GPUs. *J Supercomput*. 2013; 64(1):49-58. https://doi.org/10.1007/s11227-012-0761-2.

35. Marchesini R, Bertoni A, Andreola S, Melloni E, Sichirollo AE. Extinction and absorption coefficients and scattering phase functions of human tissues in vitro. *Applied Optics*. 1989;28 (12):2318. https://doi.org/10.1364/ao.28.002318.

36. Liesen, J. and Strakos, Z. (2013) Oxford, UK: Oxford University Press, *Krylov Subspace Methods: Principles and Analysis*.

37. Sonneveld P. CGS, a fast Lanczos-type solver for nonsymmetric linear systems. *SIAM J Sci Stat Comput*. 1989;10(1):36-52. https://doi.org/10.1137/0910004.

SUPPORTING INFORMATION

Additional supporting information may be found online in the Supporting Information section at the end of this article.